LETTER

https://doi.org/10.1038/s41586-019-1333-x

Light–wave dynamic control of magnetism

Florian Siegrist[1,2], Julia A. Gessner[1,2], Marcus Ossiander[1], Christian Denker[3], Yi-Ping Chang[1], Malte C. Schröder[1], Alexander Guggenmos[1,2], Yang Cui[2], Jakob Walowski[3], Ulrike Martens[3], J. K. Dewhurst[4], Ulf Kleineberg[1,2], Markus Münzenberg[3], Sangeeta Sharma[5] & Martin Schultze[1,6]*

The enigmatic interplay between electronic and magnetic phenomena observed in many early experiments and outlined in Maxwell's equations propelled the development of modern electromagnetism[1]. Today, the fully controlled evolution of the electric field of ultrashort laser pulses enables the direct and ultrafast tuning of the electronic properties of matter, which is the cornerstone of light-wave electronics[2–7]. By contrast, owing to the lack of first-order interaction between light and spin, the magnetic properties of matter can only be affected indirectly and on much longer timescales, through a sequence of optical excitations and subsequent rearrangement of the spin structure[8–16]. Here we introduce the regime of ultrafast coherent magnetism and show how the magnetic properties of a ferromagnetic layer stack can be manipulated directly by the electric-field oscillations of light, reducing the magnetic response time to an external stimulus by two orders of magnitude. To track the unfolding dynamics in real time, we develop an attosecond time-resolved magnetic circular dichroism detection scheme, revealing optically induced spin and orbital momentum transfer in synchrony with light-field-driven coherent charge relocation[17]. In tandem with ab initio quantum dynamical modelling, we show how this mechanism enables the simultaneous control of electronic and magnetic properties that are essential for spintronic functionality. Our study unveils light-field coherent control of spin dynamics and macroscopic magnetic moments in the initial non-dissipative temporal regime and establishes optical frequencies as the speed limit of future coherent spintronic applications, spin transistors and data storage media.

Although matter reacts to optical excitations by a virtually instantaneous and direct response of electrons to electric-field oscillations, ultrafast magnetic switching is intrinsically slower owing to the need of mediating processes linking optical excitations to spin dynamics[8,9,13,14]. Femtosecond laser pulses can modify magnetic properties at response times of several tens of femtoseconds or longer (50×10^{-15}–500×10^{-15} s)[15,16], the prospect of optical control of ferromagnetic bits has been discussed[18], and circularly polarized attosecond light pulses have been proposed to generate ultrafast magnetic-field bursts as new tools for ultrafast magneto-optics[19]. However, direct experimental evidence of the ability to link the response of a spin system to the quasi-instantaneous opto-electronic response calls for attosecond temporal resolution and has been missing until now.

A route to the novel regime of attosecond magnetism has been worked out theoretically. The proposed approach uses ferromagnetic alloys or layer stacks, where optical excitations result in the local displacement of charge carriers between different atomic species or across layer interfaces, in analogy to shift currents associated with the bulk photovoltaic effect[20]. In such a scenario, dubbed optically induced spin and orbital momentum transfer (OISTR), the spatially dislodged electron wave carries its spin away from the atomic species at which its ground state resides[17]. Consequently, the resulting coherent spin transfer is linked directly to the temporal evolution of the optical excitation field and modifies the spin moments of magnetic layers extending over macroscopic dimensions defined by the illuminated area.

Critical for advancing towards attosecond magnetism is an experimental scheme with the ability to control and detect the sub-optical-cycle evolution of electronic excitations driven by ultrafast electric fields, combined with simultaneous observation of modifications of the magnetic moments of individual sample constituents. Here we achieve this by linking attosecond transient extreme ultraviolet (XUV) absorption spectroscopy detection (attosecond XAS), which is sensitive to the temporal evolution of electronic excitations[2–7], with simultaneous attosecond time-resolved magnetic circular dichroism (attosecond MCD) (Fig. 1), which probes the local magnetic moment—both with a temporal resolution better than 1/10 of the cycle time of visible light.

In our experiment, ultrafast near-infrared (NIR) few-cycle laser pulses serve as a temporally well confined trigger of electronic excitations in nickel. The metal exhibits broadband resonant absorption properties (see density of states, DOS, in Fig. 1c) and the strong electric field of the laser pulse accelerates electrons with energies below the Fermi energy in the band structure or promotes them to states in higher-energy bands during excitation bursts phase-locked to the field maxima, leading to a stepwise increase of the number of excited carriers. Similarly, for nickel sandwiched between platinum layers, the optical excitation is a virtually instantaneous response to the oscillating external electric field. However, the adjacent heavy metal ad-layers open an additional excitation pathway where an electron is coherently driven across the material interface from states around the Fermi energy of nickel into vacant platinum states (Fig. 1c, d).

The resulting depletion of majority spins, which are oriented by placing the samples in a static external magnetic field ($B_{ext} = 50$ mT) well beyond magnetic saturation, leads to a macroscopic reduction of the magnetic moment of the nickel layer. We employ attosecond MCD, as illustrated in Fig. 1, for the first real-time study of this light-field-induced coherent modification of the magnetization of a material.

Linearly polarized attosecond pulses are generated by the same ultrafast laser pulses used to pump the electronic system of the samples via high-harmonic generation and subsequent spectral selection[21–23]. To implement a time-resolved variant of X-ray MCD detection[24], we developed a grazing-incidence, multi-reflection phase retarder[25,26] (Fig. 1a) optimized for photon energies in the XUV regime (see Methods).

In our experiment, the resulting circularly polarized attosecond pulses cover XUV photon energies around the nickel $M_{2,3}$-transition (Fig. 1) and last about 20% of the half-cycle duration of the optical pump field ($\tau_{probe} = 310$ as), as confirmed by attosecond streak-camera detection. In attosecond XAS, these pulses allow us to measure the dynamics of photo-excited electrons and modifications of the spin structure. Final-state interactions between electrons photo-injected into conduction-band states and electrons promoted into the conduction band by XUV photons turn the energy-resolved absorption into a sensitive probe for pump-laser-induced population transfer between electronic states around the Fermi edge of nickel[27].

[1]Max-Planck-Institute of Quantum Optics, Garching, Germany. [2]Fakultät für Physik, Ludwig-Maximilians-Universität München, Garching, Germany. [3]Institut für Physik, Universität Greifswald, Greifswald, Germany. [4]Max Born Institute for Nonlinear Optics and Short Pulse Spectroscopy, Berlin, Germany. [5]Max-Planck-Institute of Microstructure Physics, Halle (Saale), Germany. [6]Institute of Experimental Physics, Graz University of Technology, Graz, Austria. *e-mail: schultze@tugraz.at

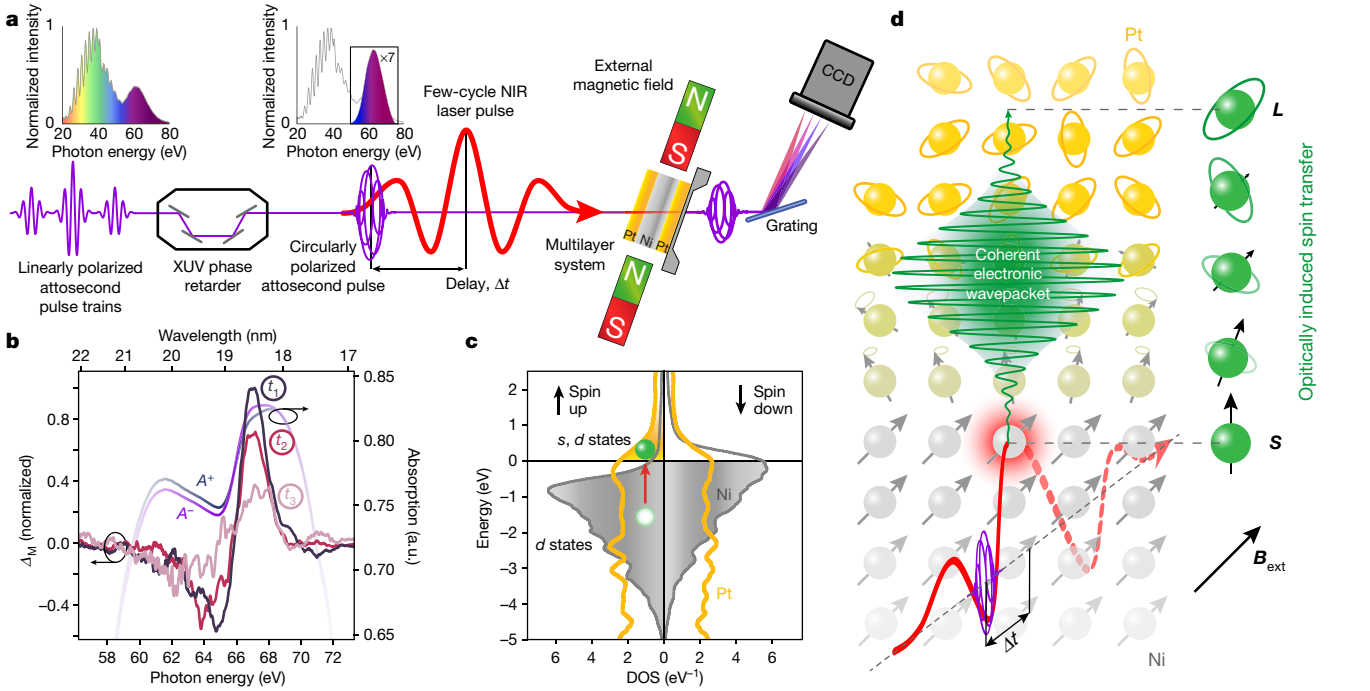

Fig. 1 | Attosecond MCD for the study of ultrafast magnetism. **a**, A quarter-wave phase retarder and band-pass filter (incident and transmitted spectra shown in the insets), optimized for photon energies covering the M-edge absorption of most transition metals, is used to turn incident linearly polarized attosecond pulse trains into isolated circular polarized attosecond pulses. These are applied as probe pulses to record the magnetic circular dichroism contrast Δ_M of nickel/platinum multilayer systems pumped by few-cycle NIR waveforms in an external magnetic field. Before the few-cycle NIR excitation, the nickel/platinum multilayer and the bulk nickel are in the magnetically saturated state along the in-plane-direction easy axis set by the external magnetic field. CCD, XUV-sensitive charge-coupled device camera. **b**, Recorded absorption A^+ and A^- for the two orientations of the magnetic field applied to the sample and the resulting attosecond MCD contrast, before the arrival of the NIR pulse (t_1), which represents the unperturbed system, shortly after its arrival (t_2) and hundreds of femtoseconds after (t_3) excitation (a.u., arbitrary units). Arrows indicate the corresponding vertical axes. **c**, **d**, In the multilayer (as opposed to bulk nickel), the optical excitation causes a coherent trans-interface charge current driven by the few-cycle light pulse, which is associated with the synchronous transfer of spin into the heavy metal**.** **c**, The grey shaded area represents occupied states in nickel, and the yellow area depicts unoccupied platinum states. Electronic excitation (red arrow) promotes an electron into the platinum layer (green circle), leaving a vacancy (empty green circle) in nickel. **d**, The NIR pump (red waveform) excites a coherent electron wavepacket (green) into the heavy metal ad-layer, where the spin experiences strong spin–orbit coupling, resulting in the circular XUV probe pulse (purple waveform) recording a decreased MCD signal.

Recording the transmitted XUV spectral intensities $I^{+/-}$ for two opposite magnetization directions oriented along the sample surface (or equivalently for two orthogonal helicities of the attosecond pulses) yields the magnetic dichroism contrast, $\Delta_M = I^+ - I^-$ (see Fig. 1b and Methods). Detection of Δ_M renders the method sensitive to element-specific local magnetic moments and enables the simultaneous tracking of sub-femtosecond modifications of both the electronic and magnetic properties induced by strong-field optical pumping.

Figure 2 shows the recorded transients of attosecond XAS and attosecond MCD. Ultrashort NIR waveforms with a central wavelength of $\lambda_{NIR} = 800$ nm, set to a peak intensity of $I_{NIR} = 4 \times 10^{12}$ W cm^{-2} and a full-width at half-maximum (FWHM) duration of $\tau_{pump} = 4$ fs (cycle time $\tau_{800\,nm} = 2.7$ fs), are used to excite electrons in nickel (Fig. 2b; see Methods for details on sample preparation and static characterization). Owing to the attosecond temporal resolution of our experiment, a repetitive decrease of the XUV absorbance is observed (red line) in synchrony with the electric-field oscillations (simulated waveform depicted as a green line at the top of Fig. 2a)[3] when the relative delay Δt between the NIR pump waveform and the attosecond probe pulse is scanned. Increased absorption (energy interval $\Delta E = 65.5$–66.5 eV) is the result of reduced Pauli blocking in electronic states gradually liberated by the pump-field-induced promotion of carriers into states above the Fermi energy. The stepwise behaviour with a rise time of <500 as is indicative of the transition rate peaking at the field crests of the light waveform and of the number of excited carriers increasing in synchrony with the half-cycle oscillations of the NIR pump laser pulses, reminiscent of interband tunnelling[3,5,28]. Inspection of the simultaneously recorded attosecond MCD contrast Δ_M (blue line) yields no observable change within the sampled time interval, indicating the conservation of magnetic moment in the ferromagnetic nickel layer for the first ~10 fs during and after electronic excitation.

In striking contrast, Fig. 2a shows that the magnetic moment of nickel sandwiched between platinum layers (see Methods), under otherwise identical experimental conditions, responds to the optical excitation as fast as the electronic system. The platinum surrounding the nickel acts as an efficient spin absorber for optical excitations transferring charge across the interfaces. In these Ni/Pt samples, ultrafast Δ_M changes (blue line) larger than 40% of the initial value are immediately discernible during the light-field oscillations that cause optical excitation, attesting to the dominant role of OISTR in the loss of magnetic moment. The reduction acts with a time constant of $\tau_{coherent} = (4.5\text{ fs}) \times (1/e)$, concurrent with the field-induced excitation and identical to the response function computed from the laser pulse duration. This synchrony is direct evidence of coherent, sub-femtosecond magnetization control extended over the macroscopic dimensions probed by the attosecond-pulse spot size of 40 μm. A periodic modulation of the attosecond MCD signal on top of the ultrafast decrease is beyond current experimental certainty and will be the subject of future studies.

To shed light on the coherent electronic processes taking place in the presence of the oscillating light field and its influence on the initial stages of ultrafast spin dynamics, we turn to theory. Established semi-classical models omit the wavepacket nature of excited electrons and correctly account for super-diffusive transport after tens

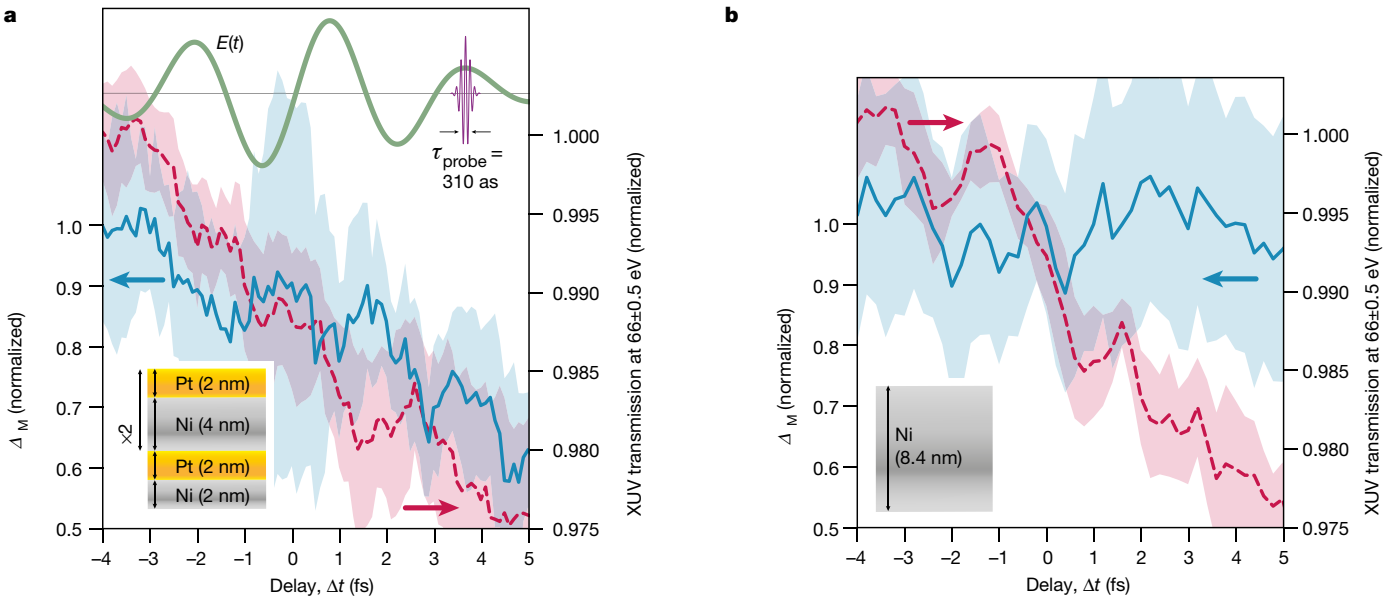

Fig. 2 | Attosecond MCD measurements of light-field-induced coherent spin transfer. a, **b**, The strong electric field $E(t)$ (waveform fitted to an attosecond streak-camera recording; green line in **a**; see Methods section) of an ultrashort laser pulse excites electrons around the Fermi energy in Ni/Pt-multilayer samples (**a**) and bulk nickel (**b**). The resulting transfer of electron population in synchrony with the laser field's half-cycle oscillations is tracked with attosecond XAS (probe pulse duration $\tau_{probe} = 310$ as) and yields a stepwise modification of the XUV transmission evaluated at 66 ± 0.5 eV (red dashed curves). The simultaneously recorded attosecond MCD contrast Δ_M, evaluated in the energy interval 66.5–68 eV, around the nickel $M_{2,3}$ edge is a measure of the magnetization of the nickel layer (blue solid curves). The reduction of the magnetic moment of the multilayer system synchronously with the electronic response provides clear experimental evidence of ultrafast coherent spin transfer and of the OISTR effect. This is supported further by the bulk nickel showing no noticeable change in magnetic moment in the first femtoseconds after excitation (**b**) while exhibiting an electronic response linked to the electric-field oscillations of the excitation pulse. Blue- and red-shaded regions indicate the standard deviation of the average along the energy dimension.

of femtoseconds have elapsed and scattering events have randomized electron momenta and energies[14]. On shorter timescales, and to describe the coherent phenomenon observed here, a dynamical and fully coherent quantum description of the laser-driven electron waves is required. To that end, we implement a state-of-the-art time-dependent density functional theory (TD-DFT; see Methods for computational details) approach that accounts for the coupled dynamics of both charge and spins, and yields the magneto-optical function, whose absorptive component is proportional to the magnetic dichroism contrast, $\Delta_M = I^+ - I^-$. Inspection of the results determines that the cross-interface flow of charge and spin currents governs the dynamics in early times (during and immediately after pumping), followed by spin–orbit-mediated spin-flips. The net result is a coherent momentum transfer in space and time across the interface by redistribution of the interlinked spin, $\boldsymbol{S}(t)$, and orbital angular momentum, $\boldsymbol{L}(t)$. The computations emphasize that coherent momentum transfer dictates the dynamics for up to five atomic layers in the vicinity of the interface, beyond which the excited charge decays rapidly[29].

The combination of state-of-the-art TD-DFT and the novel attosecond MCD technique—both of which are capable of tracking ultrafast charge and spin migration that outpace the slower lattice dynamics—is therefore a unique and powerful framework to investigate this unexplored few-femtosecond timescale on which different mechanisms combine to turn the initially coherent optical excitation into a macroscopic loss of magnetic moment. Figure 3a shows the results of the attosecond MCD recording for the magnetization dynamics in Ni and Ni/Pt sandwich samples pumped at an intensity of $I_{NIR} = 2 \times 10^{12}$ W cm^{-2} (red, nickel; blue, Ni/Pt) in comparison with the results of ab initio computations with the sample geometry and experimental laser pulse parameters as input. The loss of magnetic moment in nickel (red line, experiment; violet line, theory) mostly stalls during strong-field excitation and subsequently evolves with a demagnetization rate higher than the theoretical predictions, which are obtained in the absence of nuclear dynamics and for bulk Ni instead of a thin-film geometry.

By contrast, Ni/Pt (blue line) suffers a swift demagnetization within the pump pulse duration, and the agreement between the experimentally observed Δ_M and the calculated time evolution (including spin–orbit coupling; dark-green line) of the relative magnetic moment $M(t)/M(0)$ proves the validity of the theoretical approach and confirms that the experimental observable is a direct measure of the layer magnetization. Strikingly, excluding spin–orbit coupling from the theoretical calculations (light-green line) causes a levelling of the predicted magnetization dynamics at 20 fs, which is not mirrored in the experimental data obtained in the multilayer system. Because the only process that can cause demagnetization of Ni, apart from spin–orbit coupling, is the flow of electrons (carrying their spins) across the interface, these first 20 fs mark the hitherto unexplored time interval in which the multilayer-specific OISTR-mediated coherent momentum transfer dictates the physics of spin dynamics.

Our data indicate the presence of a second timescale of slower demagnetization (20 fs $< t <$ 50 fs), where theory determines that spin–orbit-mediated spin-flips dominate the evolution of the magnetic moment. Approximately 50 fs after optical excitation the demagnetization dynamics of both samples converge, and at longer timescales ($t >$ 70 fs, Fig. 3b) the multilayer sample fully demagnetizes with a time constant of $\tau_{incoherent} = 112 \pm 6$ fs (standard error of the mean) which represents the transition to stochastic dynamics rooted in magnetically correlated behaviour and is in good agreement with previous experiments reporting the decay of magnetic moment within 120 fs for pure nickel[15].

We report the first experimental evidence of light-wave-induced coherent transfer of spin and orbital angular momentum in space and time caused by the interplay of few-cycle optical excitation and the spin–orbit interaction in magnetic and non-magnetic multilayers. This excursion into the unexplored territory of ultrafast ($t <$ 20 fs) all-optical control of spin dynamics and macroscopic magnetic moments by (and in synchrony with) the oscillations of ultrafast electric fields opens the door to attosecond magnetism and provides a benchmark for the design

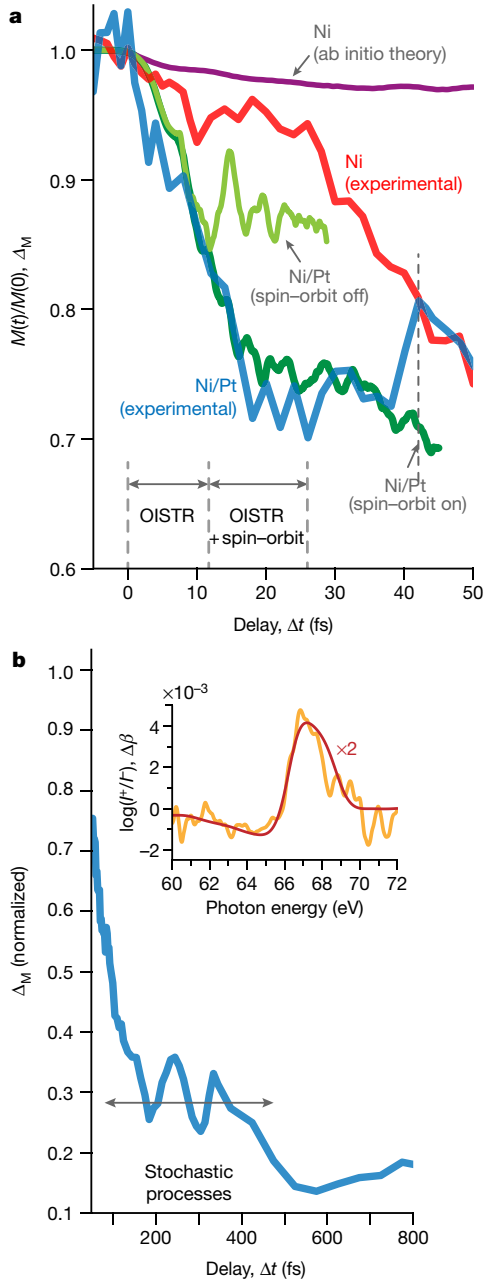

Fig. 3 | Optically induced spin-transfer, post-excitation spin dynamics and quantum dynamical modelling. a, Comparison between the experimentally recorded attosecond MCD trace in Ni/Pt-multilayers (blue line) and pure Ni (red) with the ab initio simulation of light-field-induced spin dynamics, including spin–orbit coupling in the multilayer (dark-green line) reveals that for the first 10 fs the demagnetization of Ni layers is entirely due to flow of majority-spin current across the material interface. Theoretical calculations without the spin–orbit interaction predict saturation of the demagnetization 15 fs after the optical excitation (light-green line). This is a clear indication that beyond this time all the demagnetization is caused by spin flips, whereas at earlier times spin dynamics is governed by OISTR, which is absent in the theoretical prediction for bulk nickel (violet line; see Fig. 2). **b**, Experimental data recorded for longer timescales in the multilayer system (blue line) indicate complete quenching of the magnetic moment due to stochastic processes with a characteristic timescale of 112 fs. The recorded Δ_M exhibits additional modulations up to 300 fs after the optical excitation, whose origin remains speculative, but could be rooted in coherent phonon modes affecting the coupling to the lattice. The inset compares the recorded MCD signal $\Delta = \log(I^+/I^-)$ of the Ni/Pt sandwich (orange line) with the imaginary part of the computed magneto-optical function $\Delta\beta$ (red line).

of future coherent magnetic control protocols. In tandem with the presented ab initio theory, future attosecond magnetism experiments are expected to elucidate the physical mechanisms behind spin and lattice momentum transfer and explore the role of phonons in the transition from the coherent to the thermal regime of ultrafast magnetism.

As a corollary of the reduced magnetic moment at the spin-donor sites observed here, our theory predicts that in alloys or suitably chosen multilayer systems the same mechanism can cause a local ultrafast increase in magnetic moment at spin-acceptor sites to sustain reversible optical manipulation of magnetic moments, bringing spintronics to the attosecond regime[17]. Notably, optically induced inter-site spin transfer appears as a general property of magnetic heterostructures. We anticipate the proposed experimental method and the concept of attosecond magnetism to also have a vital role in the exploration of pre-spin–orbit dynamics in coupled ferromagnetic–anti-ferromagnetic domains, systems with intertwined spin and charge orders, and other strongly correlated systems[30].

Finally, the observed sub-femtosecond magnetization control via optically induced spin transfer is promising for a new class of ultrafast spintronic applications and suggests the feasibility of light-wave-gated coherent spin transistors mimicking spintronic functionality that is orders of magnitude faster than existing applications.

Online content

Any methods, additional references, Nature Research reporting summaries, source data, statements of data availability and associated accession codes are available at https://doi.org/10.1038/s41586-019-1333-x.

Received: 16 December 2018; Accepted: 26 April 2019;
Published online 26 June 2019.

1. Ørstedt, J. C. Experimenta circa effectum conflictus electrici in acum magneticam. *J. Chem. Phys.* **29**, 275–281 (1820).
2. Schiffrin, A. et al. Optical-field-induced current in dielectrics. *Nature* **493**, 70–74 (2013); addendum **507**, 386–387 (2014).
3. Schultze, M. et al. Attosecond band-gap dynamics in silicon. *Science* **346**, 1348–1352 (2014).
4. Mashiko, H., Oguri, K., Yamaguchi, T., Suda, A. & Gotoh, H. Petahertz optical drive with wide-bandgap semiconductor. *Nat. Phys.* **12**, 741–745 (2016).
5. Lucchini, M. et al. Attosecond dynamical Franz–Keldysh effect in polycrystalline diamond. *Science* **353**, 916–919 (2016).
6. Garg, M. et al. Multi-petahertz electronic metrology. *Nature* **538**, 359–363 (2016).
7. Reimann, J. et al. Subcycle observation of lightwave-driven Dirac currents in a topological surface band. *Nature* **562**, 396–400 (2018).
8. Bigot, J.-Y., Vomir, M. & Beaurepaire, E. Coherent ultrafast magnetism induced by femtosecond laser pulses. *Nat. Phys.* **5**, 515–520 (2009).
9. Boeglin, C. et al. Distinguishing the ultrafast dynamics of spin and orbital moments in solids. *Nature* **465**, 458–461 (2010).
10. Walowski, J. & Münzenberg, M. Ultrafast magnetism and THz spintronics. *J. Appl. Phys.* **120**, 140901 (2016).
11. Koopmans, B. et al. Explaining the paradoxical diversity of ultrafast laser-induced demagnetization. *Nat. Mater.* **9**, 259–265 (2010).
12. Hellman, F. et al. Interface-induced phenomena in magnetism. *Rev. Mod. Phys.* **89**, 025006 (2017).
13. Kirilyuk, A., Kimel, A. V. & Rasing, T. Ultrafast optical manipulation of magnetic order. *Rev. Mod. Phys.* **82**, 2731–2784 (2010).
14. Battiato, M., Carva, K. & Oppeneer, P. M. Superdiffusive spin transport as a mechanism of ultrafast demagnetization. *Phys. Rev. Lett.* **105**, 027203 (2010).
15. Stamm, C. et al. Femtosecond modification of electron localization and transfer of angular momentum in nickel. *Nat. Mater.* **6**, 740–743 (2007).
16. Rudolf, D. et al. Ultrafast magnetization enhancement in metallic multilayers driven by superdiffusive spin current. *Nat. Commun.* **3**, 1037 (2012).
17. Dewhurst, J. K., Elliott, P., Shallcross, S., Gross, E. K. U. & Sharma, S. Laser-induced intersite spin transfer. *Nano Lett.* **18**, 1842–1848 (2018).
18. Lambert, C.-H. et al. All-optical control of ferromagnetic thin films and nanostructures. *Science* **345**, 1337–1340 (2014).
19. Bandrauk, A. D., Guo, J. & Yuan, K.-J. Circularly polarized attosecond pulse generation and applications to ultrafast magnetism. *J. Opt.* **19**, 124016 (2017).
20. Laman, N., Bieler, M. & van Driel, H. M. Ultrafast shift and injection currents observed in wurtzite semiconductors via emitted terahertz radiation. *J. Appl. Phys.* **98**, 103507 (2005).
21. Hentschel, M. et al. Attosecond metrology. *Nature* **414**, 509–513 (2001).
22. Schweinberger, W. et al. Waveform-controlled near-single-cycle milli-joule laser pulses generate sub-10 nm extreme ultraviolet continua. *Opt. Lett.* **37**, 3573–3575 (2012).

23. Fieß, M. et al. Versatile apparatus for attosecond metrology and spectroscopy. *Rev. Sci. Instrum.* **81**, 093103 (2010).
24. Carra, P., Thole, B. T., Altarelli, M. & Wang, X. X-ray circular dichroism and local magnetic fields. *Phys. Rev. Lett.* **70**, 694–697 (1993).
25. Höchst, H., Patel, R. & Middleton, F. Multiple-reflection $\lambda 4$ phase shifter: a viable alternative to generate circular-polarized synchrotron radiation. *Nucl. Instrum. Meth. A* **347**, 107–114 (1994).
26. Willems, F. et al. Probing ultrafast spin dynamics with high-harmonic magnetic circular dichroism spectroscopy. *Phys. Rev. B* **92**, 220405 (2015).
27. Kaindl, G., Brewer, W. D., Kalkowski, G. & Holtzberg, F. M-edge X-ray absorption spectroscopy: a new tool for dilute mixed-valent materials. *Phys. Rev. Lett.* **51**, 2056–2059 (1983).
28. Ghimire, S. et al. Strong-field and attosecond physics in solids. *J. Phys. B* **47**, 204030 (2014).
29. Dewhurst, J. K., Shallcross, S., Gross, E. K. U. & Sharma, S. Substrate-controlled ultrafast spin injection and demagnetization. *Phys. Rev. Appl.* **10**, 044065 (2018).
30. Li, T. et al. Femtosecond switching of magnetism via strongly correlated spin-charge quantum excitations. *Nature* **496**, 69–73 (2013).

Acknowledgements We acknowledge infrastructural support by F. Krausz. This work was supported by the Max Planck Society, the Deutsche Forschungsgemeinschaft Cluster of Excellence: Munich Centre for Advanced Photonics (http://www.munich-photonics.de), the Deutsche Forschungsgemeinschaft CRC/Transregio 227 (Project A04) and the US Air Force Office of Scientific Research under award number FA9550-16-1-0073.

Reviewer information *Nature* thanks Marie Barthelemy, Ilias Perakis and the other anonymous reviewer(s) for their contribution to the peer review of this work.

Author contributions M.S., S.S. and M.M. designed and initiated the study. Experiments were performed by F.S., J.A.G., M.O., M.C.S., Y.-P.C. and M.S. Sample design and preparation were carried out by C.D., U.M., J.W. and M.M. Theoretical investigations were conducted by S.S. and J.K.D. Design and manufacturing of XUV optics were carried out by A.G., Y.C., M.S. and U.K. The manuscript was written by M.M., M.S. and S.S.; all authors discussed the results and contributed to the manuscript.

Competing interests The authors declare no competing interests.

Additional information
Extended data is available for this paper at https://doi.org/10.1038/s41586-019-1333-x.
Reprints and permissions information is available at http://www.nature.com/reprints.
Correspondence and requests for materials should be addressed to M.S.
Publisher's note: Springer Nature remains neutral with regard to jurisdictional claims in published maps and institutional affiliations.

METHODS

Theory. Computations rely on the Runge–Gross theorem[31], which establishes that the time-dependent external potential is a unique functional of the time-dependent density, given the initial state. On the basis of this theorem, a system of non-interacting particles can be chosen such that its density is equal to that of the interacting system at all times. The wave function is represented as a Slater determinant of single-particle Kohn–Sham (KS) orbitals. A fully non-collinear spin-dependent version of this theorem entails that these KS orbitals are two-component Pauli spinors determined by the equations:

$$i\frac{\partial\psi_j(\boldsymbol{r},t)}{\partial t}=\left\{\frac{1}{2}\left[-i\nabla+\frac{1}{c}\boldsymbol{A}_{\mathrm{ext}}(t)\right]^2+v_s(\boldsymbol{r},t)+\frac{1}{2c}\boldsymbol{\sigma}\cdot\boldsymbol{B}_s(\boldsymbol{r},t)\right.$$
$$\left.+\frac{1}{2c}\boldsymbol{\sigma}\cdot(\nabla v_s(\boldsymbol{r},t)\times -i\nabla)\right\}\psi_j(\boldsymbol{r},t) \quad (1)$$

where the first term is the kinetic term, responsible for the flow of current across the interface[32], $\boldsymbol{A}_{\mathrm{ext}}(t)$ is a vector potential representing the applied laser field, and σ are the Pauli matrices. The KS effective potential $v_s(\boldsymbol{r},t) = v_{\mathrm{ext}}(\boldsymbol{r},t) + v_{\mathrm{H}}(\boldsymbol{r},t) + v_{\mathrm{XC}}(\boldsymbol{r},t)$ is decomposed into the external potential, $v_s(\boldsymbol{r},t)$, the classical electrostatic Hartree potential, $v_{\mathrm{H}}(\boldsymbol{r},t)$, and the exchange-correlation potential, $v_{\mathrm{XC}}(\boldsymbol{r},t)$. Similarly, the KS magnetic field is written as $\boldsymbol{B}_s(\boldsymbol{r},t) = \boldsymbol{B}_{\mathrm{ext}}(\boldsymbol{r},t) + \boldsymbol{B}_{\mathrm{H}}(\boldsymbol{r},t) + \boldsymbol{B}_{\mathrm{XC}}(\boldsymbol{r},t)$, where $\boldsymbol{B}_{\mathrm{ext}}(\boldsymbol{r},t)$ is the magnetic field of the applied laser pulse, plus possibly an additional magnetic field, and $\boldsymbol{B}_{\mathrm{XC}}(\boldsymbol{r},t)$ is the exchange-correlation magnetic field. The final term is the spin–orbit coupling term, the presence of which ensures that the total spin angular momentum, $\boldsymbol{S}$, is not a good quantum number and hence spin-flip excitations can lead to loss in $\boldsymbol{S}$. Equation (1) is solved for the electronic system alone in dipole approximation and using an adiabatic local spin-density approximation[33] for the exchange-correlation fields. The dynamics of the nuclear degrees of freedom and radiative effects, described by simultaneously time-propagating Maxwell's equations, are not included in the present work, limiting the predictive power of the method to the first ~100 fs during and after pumping.

Calculations of a magneto-optical function for the Ni/Pt layer (see inset of Fig. 3) were performed by a three-step process: (i) the ground state of Ni/Pt multilayers was determined using DFT; (ii) a fully spin-polarized many-body calculation[34] was performed, expanding the self-energy in terms of the single-particle Green function G and the screened Coulomb interaction W (GW approximation), to determine the correct position and width of Ni 3p states; and (iii) the response function was calculated on top of the GW-corrected KS ground state. This response function was calculated within linear-response TD-DFT, in which the excitonic effects[35] and local field effects can be easily included. An advantage of this treatment is that no experimental parameter was needed to determine accurate magneto-optical functions.

Computational details. For a periodic sequence of three monolayers of Ni on seven monolayers of Pt, a fully non-collinear version of TD-DFT, as implemented within the Elk code[36], was used for all calculations presented here. All the computations were done using the state-of-the art full-potential linearized augmented plane wave (LAPW) method. The computational cost prohibited inclusion of more monolayers in the calculation. The results presented for Ni/Pt required approximately 270,000 processor hours.

A regular $8 \times 8 \times 8$ mesh in momentum space and a time step of $\Delta t = 2$ as were used for the time-propagation algorithm. To mimic the experimental resolution, a Gaussian energy broadening with a spectral width of 0.027 eV was applied. The laser pulse used in the present work was linearly polarized (out-of-plane polarization) with a central frequency of 1.55 eV, an FWHM duration of 8 fs and a fluence of 5.4 mJ cm^{-2}.

Experiment. The experiments were carried out with a phase-stabilized few-cycle NIR laser as the driver (FemtoPower), emitting pulses with duration of 4 fs and pulse energy of 0.5 mJ at a repetition rate of 4 kHz. These pulses were focused into a neon-filled ceramic target, generating high-harmonic radiation with a cut-off energy of around 70 eV. A Mach–Zehnder-type interferometer was used to introduce a delay between the NIR and the XUV pulses. We used a 150-nm Al filter to block the driving NIR laser pulse while providing a constant transmission at the energies of interest. Isolated attosecond pulses were achieved by spectrally filtering the cut-off regime with a Si/B_4C multilayer mirror with a reflectivity of 15% at 66 eV and an FWHM bandwidth of 8 eV for an angle of incidence of 45°. Subsequently, the multi-reflection phase-shifter changed the polarization from linear to elliptical. An ellipticity of $\varepsilon > 0.75$ was achieved with transmittance >25% and without introducing substantial wavelength dispersion.

Four Mo/B_4C multilayer mirrors were mounted at an angle of 78° with respect to the surface normal—a setting optimized for high broadband transmission and maximized ellipticity. With that setting, laser-based MCD measurements at M-edge transitions can be used to time-track magnetization dynamics, as an extension of the methodology developed at synchrotron sources and employing L-edge transitions in the past.

The bandwidth covered by the circular polarized attosecond pulses permitted us to probe the Ni M-edge transitions M_2 and M_3 at 68 eV and 66.2 eV, respectively[37]. For our samples, these resonant transitions caused a 20% reduction in transmission, in addition to the non-resonant background[38]. In principle, the Pt O_2 transition at 65.3 eV was also covered by the bandwidth of the attosecond pulses. Owing to the considerably smaller transition strength compared to the Ni resonances and the extended bandwidth of almost 10 eV of the Pt O_2 edge, our experiment was not capable of resolving this contribution. Future studies in suitably chosen heterostructures (for example, iron–cobalt or nickel–cobalt multilayers or Heusler compounds) will be designed to allow resolving the anti-phase magnetization dynamics due to OISTR in such systems, where XUV resonances of both constituents can be tracked. To maximize the MCD contrast while maintaining sufficient XUV transmission, the samples were mounted at an angle of ~35° between the propagation direction of the laser and the surface normal. The surface normal and the magnetization direction of the sample were on a plane parallel to the propagation direction of the laser field. We used a gold-coated grating with 2105 lines per millimetre in reflection geometry (Jobin–Yvon) with a 200-μm entrance slit as a spectrometer.

For every delay step, we measured the transmitted spectra for both magnetization directions of the sample and then scanned the delay over the region of interest. To check and compensate for long-timescale drifts in the XUV spectrum, we took spectra of the transmitted XUV light in the absence of the NIR laser light before and after every scan to ensure that no irreversible changes were made to the multilayer or the supporting polycrystalline silicon substrate.

We observed the OISTR effect for pump light intensities of $I_{\mathrm{NIR}} = (1.5–4) \times 10^{12}$ W cm^{-2}. At lower intensities, only the slow demagnetization component depicted in Fig. 3b was observed. At intensities of $I_{\mathrm{NIR}} > 5 \times 10^{12}$ W cm^{-2} the time span between laser pulses (250 μs) was found to be insufficient for the magnetic system to return to the unperturbed state.

To explore the sub-optical cycle dynamics, the data displayed in Fig. 2 were recorded with a delay step size of 0.1 fs and an integration time of 20 s per time step and magnetization direction for a total scan duration of 9 fs, which extends well beyond the FWHM duration of the NIR pump waveform (4 fs). For each time step an additional absorption spectrum was recorded without the pump light impinging on the sample. A running average was applied along the delay dimension with a range of 5 (10) time steps for the attosecond XAS (attosecond MCD) data, respectively. An evaluation using artificial data with random noise added yielded an estimated temporal resolution of <300 as (<800 as).

The total scan time was >2 h, limited by the long-term stability of the laser's carrier-envelope phase locking and the pump–probe interferometer reproducibility, effectively confining the obtainable delay scan range to 10 fs (0.1 fs step size) and 200 fs (2 fs step size).

The attosecond MCD signal was extracted from a series of two recordings with the direction of the external magnetic field (that is, the magnetization direction of the sample) reversed. For the practical reasons detailed earlier, the maximum feasible integration time per spectrum was 20 s. Extended Data Fig. 2 shows the fidelity with which the attosecond MCD signal can be obtained as a function of integration time.

Data evaluation. For the energy calibration of our spectrum we used the pronounced Al $L_{2,3}$ edges at 72.7 eV and the Ni M_3 edge at 66.2 eV. The grating equation $\lambda = d(\sin\theta_i - \sin\theta_f)$ (where λ denotes the wavelength, d the distance between the grating and the detector, θ_i the angle between the incident beam and the surface normal of the grating and θ_f the angle between the surface normal of the grating and the refracted beam) gives the relation between the position of a spectral feature detected by the XUV-sensitive CCD camera (Princeton Instrument PIXIS) and the photon energy. We investigated the influence of the non-homogeneous diffraction and reflection efficiency of the grating and found it to be negligible within the photon energy range relevant in this study.

We applied an equal-weight sliding average to the spectrograms along the energy ($\Delta E = 50$ meV) and the delay ($\Delta t = 0.5$ fs) dimensions. We determined the magnetic dichroism contrast according to $\Delta_M = I^+ - I^-$. Application of alternative definitions of the contrast and computation of the magnetic dichroism asymmetry had no influence on the transient signals.

$E(t)$ was obtained in an attosecond streak-camera experiment independent of the attosecond XAS/attosecond MCD recording shown in Fig. 2 (but under otherwise identical experimental conditions)[39]. Because XAS measures the action of $E(t)$ (the number of excited carriers as a function of time), the electric-field evolution is encoded in the XAS trace (which is proportional to $\int|E(t)|$)[3,39], allowing to link the relative time axis of the two experiments.

Sample preparation and magnetic characterization. A number of Ni and Ni/Pt multilayer films were grown on Si membranes and optimized to grow in an fcc structure. The 8.4-nm-thick Ni film and the Pt(2 nm)/2×[Ni(4 nm)/Pt(2 nm)]/Ni(2 nm)

multilayer were deposited on 200-nm-thick polycrystalline Si membranes (Norcada) at room temperature by electron beam evaporation under ultrahigh-vacuum conditions with a base pressure lower than 1×10^{-9} mbar and high-purity source materials (99.95%). The individual layer thicknesses in the two [Ni(4 nm)/Pt(2 nm)] bi-layers were optimized to: (i) increase the number of active interfaces for OISTR; (ii) maintain sufficient XUV transmittance and provide maximized attosecond MCD contrast; and (iii) ensure homogeneous in-plane magnetization. The sample was protected by an inert 2-nm-thick Pt capping layer, and a 2-nm-thick Ni seed layer (non-magnetic at room temperature) was grown on the substrate to provide identical surroundings to all of the Pt layers and ensure uniform growth of the layer stack. Both materials were grown in fcc structure. The deposition rate was monitored by a calibrated standard quartz crystal microbalance and adjusted to 0.02 nm s^{-1}. Special care was taken to use low-tension mounting to protect the membranes from any mechanical stress. The in-plane magnetic properties were characterized by a standard longitudinal magneto-optical Kerr effect (MOKE) setup with a 3-mW HeNe continuous-wave laser, a photoelastic modulator and Glan–laser prisms in longitudinal geometry. Measurements on both the frame and the samples' membrane window yielded similar ferromagnetic properties. For both types of samples, we found coercive fields of a few millitesla and a remanence of around 60%–70% of the saturation magnetization. MOKE measurements confirmed the absence of ferromagnetism in the nickel seed layer at room temperature, verifying that that layer did not affect the magnetic moment of the sample; see Extended Data Fig. 1. Sample production, shipping and experiments were performed under vacuum to prevent oxidation. Nevertheless, we confirmed that no change of the MOKE signal occurred after 48 h of exposure of the samples to air, ensuring that the ferromagnetic properties persisted and did not suffer from oxidic passivation of the sample surface.

Data availability

The data that support the findings of this study are available from the corresponding author upon request.

31. Runge, E. & Gross, E. K. U. Density-functional theory for time-dependent systems. *Phys. Rev. Lett.* **52**, 997–1000 (1984).
32. Krieger, K. et al. Ultrafast demagnetization in bulk versus thin films: an ab initio study. *J. Phys. Condens. Matter* **29**, 224001 (2017).
33. von Barth, U. & Hedin, L. A local exchange-correlation potential for the spin polarized case. *J. Phys. C* **5**, 1629–1642 (1972).
34. Hedin, L. New method for calculating the one-particle Green's function with application to the electron-gas problem. *Phys. Rev.* **139**, A796–A823 (1965).
35. Sharma, S., Dewhurst, J. K., Sanna, A. & Gross, E. K. U. Bootstrap approximation for the exchange-correlation kernel of time-dependent density-functional theory. *Phys. Rev. Lett.* **107**, 186401 (2011).
36. Dewhurst, K. et al. The Elk FP-LAPW code. http://elk.sourceforge.net/ (2018).
37. Fuggle, J. C. & Mårtensson, N. Core-level binding energies in metals. *J. Electron. Spectrosc.* **3**, 275–281 (1980).
38. Henke, B. L., Gullikson, E. M. & Davis, J. C. X-ray interactions: photoabsorption, scattering, transmission, and reflection at $E = 50$–$30{,}000$ eV, $Z = 1$–92. *At. Data Nucl. Data Tables* **54**, 181–342 (1993).
39. Schultze, M. et al. Controlling dielectrics with the electric field of light. *Nature* **493**, 75–78 (2013).

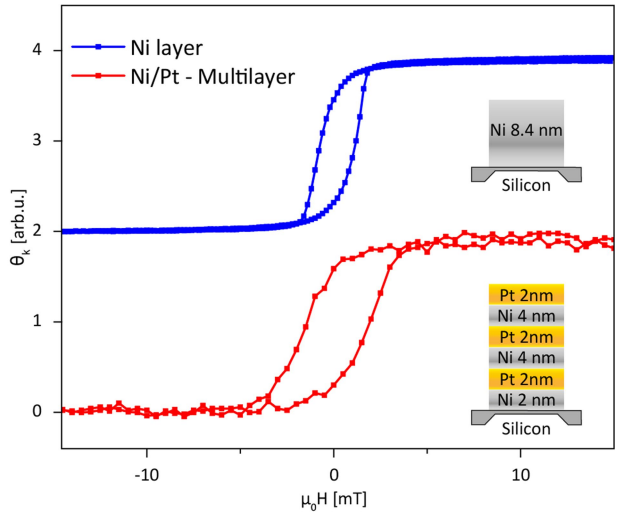

Extended Data Fig. 1 | Hysteresis of the longitudinal magneto-optical Kerr effect for nickel and Ni/Pt multilayers. The Kerr rotation angle, θ_k, is shown as a function of the applied external magnetic field, $\mu_0 H$ (μ_0, magnetic constant). Both samples (blue, Ni; red, Ni/Pt multilayer) exhibit soft magnetic hysteresis and low saturation fields, which are needed to orient the macroscopic magnetization in the sample plane.

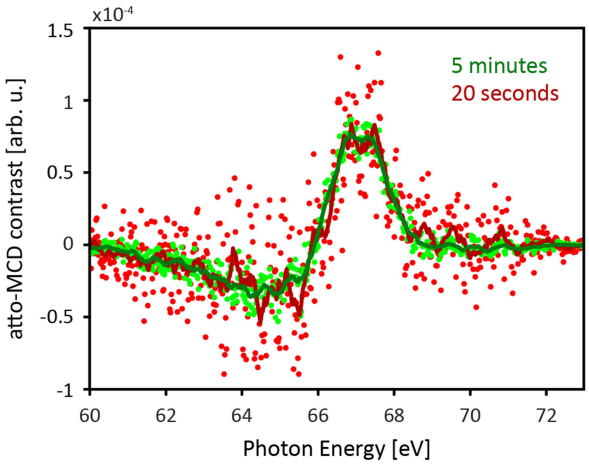

Extended Data Fig. 2 | Fidelity of attosecond MCD. Results are shown for an integration time of 300 s (green dots, individual data points; green line, moving average from 7 data points) and 20 s (red dots, individual data points; red line, moving average from 7 data points).